

# The influence of merger and convection on an anticyclonic eddy trapped in a bowl

Charly de Marez <sup>a,\*</sup>, Mathieu Le Corre <sup>a,c</sup>, Jonathan Gula <sup>a,b</sup>

<sup>a</sup> Univ. Brest, Laboratoire d'Océanographie Physique et Spatiale (LOPS), IUEM, Rue Dumont D'urville, 29280 Plouzané, France

<sup>b</sup> Institut Universitaire de France (IUF), France

<sup>c</sup> LEGOS, University of Toulouse, IRD, CNRS, CNES, UPS, Toulouse, France

## ARTICLE INFO

### Keywords:

Mesoscale

Vortex

Merger

Convection

## ABSTRACT

We investigate the impact of several parameters on the lifecycle of an anticyclonic eddy lying in a topographic depression (a bowl), similar to the Lofoten Vortex and the Rockall Trough eddy cases. We observe that the vortex merger with submesoscale coherent vortices generated at depth allows the eddy to grow in size, and intensify at depth. Wintertime convection is also shown to directly intensify the eddy by deepening isopycnals. Also, convection indirectly affects the shape of the eddy. It enhances the number of merger (1) at the surface, with small vortices generated in the convectively-deepened surface mixed-layer, and (2) at depth, because the vertical distance between the main eddy's core and small companion vortices is reduced, thus increasing the merging efficiency. These processes altogether contribute to the maintaining of the eddy. On the other hand, the bottom drag is the main process contributing to the decay of the eddy. Our study thus shows that the sustaining for several years of such eddies trapped in a bowl is mainly due to the balance between merger and bottom drag.

## 1. Introduction

Mesoscale eddies are a prominent feature of the ocean circulation. They have a strong influence on biological activity (Chelton et al., 2011), tracer transport (Zhang et al., 2014), and physical and chemical properties of the water column (Dong et al., 2014). In some regions, semi-permanent eddies can be seen throughout the year, at a nearly constant position. Among other examples, two particular cases are the Lofoten Vortex (LV), and the Rockall Trough eddy (RT eddy). These two semi-permanent eddies have the peculiarity to be anticyclonic, and located above a topographic depression – a bowl. The formation of such vortices has recently been examined by Solodoch et al. (2021). Authors showed using idealized simulations that successive merging events form a permanent anticyclone lying in the topographic depression. The dynamics of the resulting vortex depends on the ratio of eddy's vorticity to topography's potential vorticity. However, the mechanisms that sustain semi-permanent anticyclones in bowl-like topography such as the LV and the RT eddy are not yet fully understood.

The LV can be found in the Lofoten Basin in the Nordic Seas. It appears as a large anticyclone at the center of the basin. It was first detected by *in situ* data between 1970 and 1990 (Ivanov and Korablev, 1995). The LV is intensified between 700 and 900 m depth and has a radius of about 30 km (Yu et al., 2017). Two processes are candidate to explain the long lifetime of the LV. First, from observational data, Ivanov and Korablev (1995) and Bosse et al. (2019)

argued that wintertime intensification resulting from convection plays a determinant role in sustaining the LV. Second, model studies showed that the LV is sustained by the merger and alignment with smaller vortices generated by unstable boundary currents (Köhl, 2007; Trodahl et al., 2020). In the current state of knowledge, the relative importance of each process is not clear. One of the aims of the present study is to give new answers to this question.

The RT eddy is located in the Rockall Trough, off Ireland in the North Atlantic. It has a clear signature at the sea surface (Heywood et al., 1994; White and Heywood, 1995; Volkov, 2005; Xu et al., 2015), but also at depth with high values of eddy available potential energy (Roulet et al., 2014). This eddy is less sampled than the LV and less known. However, thanks to recent *in situ* deployments, it has been shown that it is intensified at depth, with a maximum azimuthal velocity of  $\sim 0.3 \text{ m s}^{-1}$  near 500 m depth (Smilanova et al., 2020). It has a radius of approximately 40 km and can reach down to 1500 m. Its lifecycle, as well as the mechanisms that sustain it are yet poorly documented. However, recent model studies by Le Corre et al. (2019) and Smilanova et al. (2020) have shown some evidences that (1) the RT eddy formation is the result of successive mergers of deeply generated submesoscale vortices along the Porcupine Bank, (2) the merger of the RT eddy with these small vortices as well as wintertime convection sustain the RT eddy, and allow it to remain semi-permanent in the Rockall Trough.

\* Corresponding author.

E-mail address: [charly.demarez@univ-brest.fr](mailto:charly.demarez@univ-brest.fr) (C. de Marez).

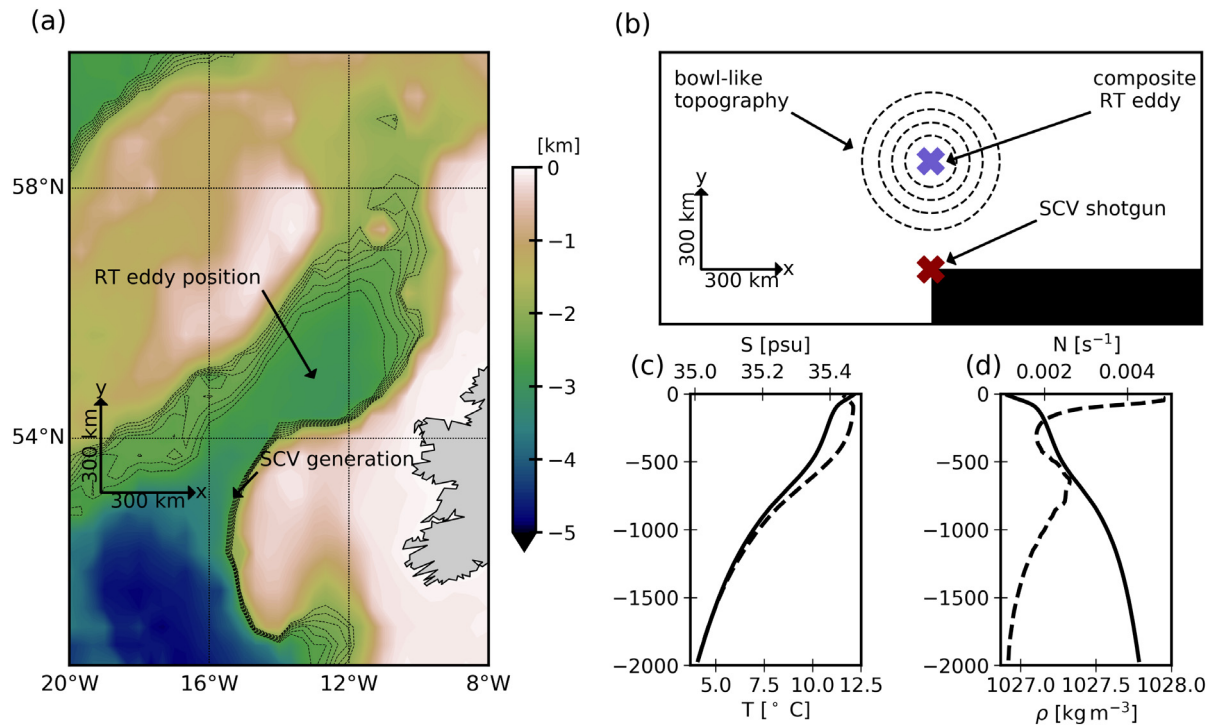


**Fig. 1.** (a) Rockall Trough bathymetry; dashed contours show isobaths 2500 to 2000 m depth with a 100 m interval. (b) Scheme of idealized simulation setup; dashed contours show same isobaths as in (a). (c) Climatological background temperature (solid) and salinity (dashed) used in idealized simulations. (d) Climatological background potential density (solid) and corresponding Brunt–Väisälä frequency (dashed) used in idealized simulations.

In this paper, we investigate the impact of several parameters on the lifecycle of an anticyclonic eddy lying in a topographic depression. In particular, we discuss the impact of merger and convection on the lifetime and shape of the anticyclone. To explore the parameter space, we use an idealized approach based on the Rockall Trough Eddy case. This allows to (1) discuss on the general behavior of anticyclonic eddies in a bowl, and (2) give insights in the particular case of the Rockall Trough Eddy that is yet poorly documented. In Section 2 we present the methods, the numerical simulation setup and the diagnostics performed on outputs. In Section 3 we present the results of our study, the impact of the different parameters on the vortex dynamics. In Section 4 we summarize and discuss the results.

## 2. Methods

### 2.1. The numerical simulations

In this section, we present the idealized simulations performed for this study. The aim of these simulations is to simulate schematically the dynamics occurring in the Rockall Trough area: a semi-permanent anticyclone (the RT eddy) lying in a bowl-like topography, fed by anticyclonic Submesoscale Coherent Vortices (SCVs) generated hundreds of kilometers away from the main eddy (hereafter, the main eddy designates the eddy that lies approximately in the center of the bowl-like topography, and merges with smaller SCVs). We detail each aspect of the simulation in the following subsections.

#### 2.1.1. Numerical setup and domain

The simulations rely on a 3D primitive equation framework. They are performed using the Coastal and Regional Ocean CCommunity model CROCO (Shchepetkin and McWilliams, 2005). This model solves the hydrostatic primitive equations for the velocity, temperature, and salinity, using a full equation of state for seawater (Shchepetkin and McWilliams, 2011). The simulations integrate the primitive equations for about 7 and a half years. The numerical settings are similar

to previous simulations performed in an idealized context (see, e.g., Méneguen et al., 2018): horizontal advection terms for tracers and momentum are discretized with fifth-order upwind advection schemes (UP5); the explicit horizontal viscosity and diffusivity are set to zero, since the UP5 scheme damps dispersive errors; the vertical advection is discretized with a fourth-order centered parabolic spline reconstruction (Splines scheme). Further discussion about these parameterizations can be found in Klein et al. (2008) or Méneguen et al. (2018). Vertical mixing of tracers and momentum is done using a K-profile parameterization (KPP, Large et al., 1994), and the effect of bottom friction is parameterized through a logarithmic law of the wall (with the same parameters than in e.g. Gula et al. (2015) or Le Corre et al. (2020)). Some simulations are run without this bottom drag to study its impact on the vortex dynamics. Simulations have 64 terrain-following vertical levels, which are stretched such that the resolution increases in the depth range where the main eddy lies, giving  $\Delta z \sim 20$  m from surface to 1000 m depth, and  $20 < \Delta z < 90$  m below. The horizontal resolution is  $\Delta x = 5$  km.

The domain is chosen so that it represents schematically the RT area, see Fig. 1(a,b). The domain is 2000 km and 1000 km wide zonally and meridionally, respectively. A bowl-like topography is placed at the center of the domain, to represent the RT topographic depression. It is modeled by a Gaussian function

$$h = h_0 + h_1 \exp(-r^2/(2R)^2),$$

with  $r = \sqrt{(x - x_0)^2 + (y - y_0)^2}$ ,  $x_0 = 1000$  km,  $y_0 = 600$  km,  $R = 100$  km,  $h_0 = 2000$  m, and  $h_1 = 500$  m, such that the simulation is 2000 m deep everywhere, except in the bowl where it reaches 2500 m deep. The background stratification is the average stratification in the RT area, see Fig. 1(c,d). It is defined as the average stratification in the RT from Le Corre et al. (2020)'s simulation. A return to this background stratification is set in the boundaries. At these boundaries a 10 km wide sponge layer avoid the generation of spurious boundary dynamics.

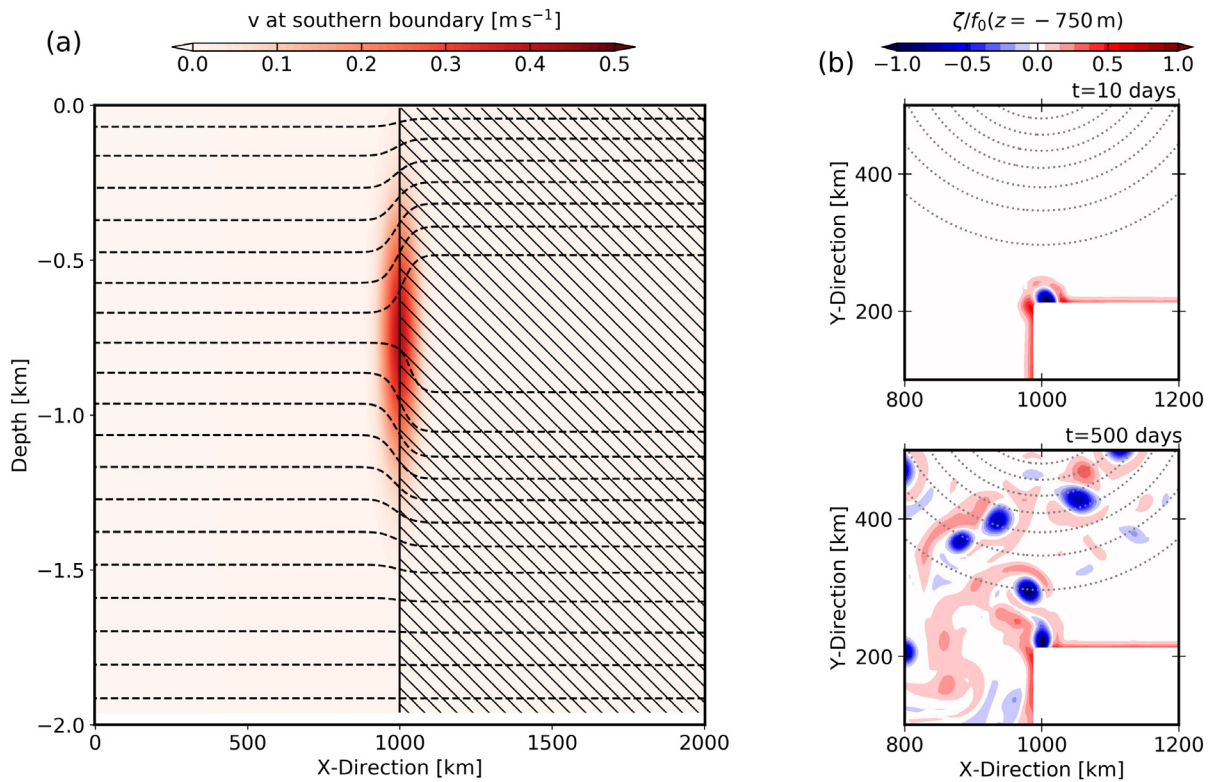


**Fig. 2.** (a) Meridional velocity at the southern boundary for the “middle” case; black lines indicate isopycnals with a  $0.5 \text{ kg m}^{-3}$  spacing; hatched area indicate the position of the mask. (b) Snapshots of normalized relative vorticity at  $t = 10$  and  $t = 500$  days, at  $750 \text{ m}$  depth, showing the SCV generation at the mask corner in the “middle” case.

### 2.1.2. The SCV shotgun

In the RT, SCVs are generated along the Porcupine Bank (Smilenova et al., 2020). To simulate this SCV generation, we designed a “SCV shotgun”, that continuously generates SCVs at a given depth during the simulation. It is placed at 300 km from the bowl-like topography center. This distance is chosen so that it is similar to the one between the Porcupine Bank and the RT eddy position in reality, see Fig. 1(a,b).

The SCV shotgun is based on the principle fully described in Deremble et al. (2016): at boundary singularities such as corners, vorticity is injected into the domain even for free-slip boundary conditions. We add a land mask forming a corner (*i.e.* a boundary singularity) at the south of the domain, with a free-slip condition along this mask. Then, we impose a meridional current at depth along the mask (see Fig. 2(a)), of the form:

$$v = v_0 \exp(-(x - x_0)^2/(2L)^2) \exp(-(z - z_0)^2/(2H)^2),$$

with  $v_0 = 0.4 \text{ m s}^{-1}$ ,  $L = 30 \text{ km}$ , and  $H = 200 \text{ m}$ . As discussed in Deremble et al. (2016), the horizontal extension and intensity of generated SCVs are mainly controlled by the sub-grid parameterization and horizontal discretization, such that  $L$  and  $v_0$  poorly control the shape of SCVs. After sensitivity tests, we chose the aforementioned values for  $v_0$ ,  $L$ , and  $H$  such that the model stability is satisfying, and that the properties and the frequency of generation of SCVs are similar to the one observed in realistic simulations of the Rockall Trough (Smilenova et al., 2020), *i.e.* about 10 SCVs are generated each year. We also vary  $z_0 = [-1250, -1000, -750, -500, -250] \text{ m}$ , to discuss the impact of the SCV depth on the merging process. They are called “deep”, “middle deep”, “middle”, “middle surf”, and “surf” cases respectively in the following. Note that the middle case is the one representative of RT SCV generation (see *e.g.* Fig. 11 in Smilenova et al. (2020)). This current is geostrophically adjusted with the density field at the southern boundary, see Fig. 2(a). Examples of SCV generation in the middle case are shown in Fig. 2(b,c).

### 2.1.3. The Rockall Trough anticyclone

As discussed in the introduction, a semi-permanent anticyclonic eddy is present in the RT throughout the whole year: the RT eddy. To simulate this presence, we add in some simulations, at initialization, a composite anticyclone representative of the RT eddy above the center of the bowl-like topography (at  $x = x_0$  and  $y = y_0$ , the blue cross position in Fig. 1(b)).

This composite was extracted from a realistic simulation representing the Subpolar North Atlantic gyre. It is fully described in Le Corre et al. (2020). The 2011 vertical properties of the simulated RT eddy being close to ship-board Conductivity–Temperature–Depth (CTD) data collected in January 2011 (see the supplementary material of Smilenova et al. (2020)), this simulation is assumed to represent well the RT eddy dynamics. An example of RT eddy occurrence in the simulation is shown in Fig. 3(a). We tracked the RT eddy by following the maximum SSH value in the area. After isolating the eddy, we took its temporal main structure and azimuthally averaged it to obtain the main composite structure of the RT eddy (Fig. 3(b,c,d,e)).

### 2.1.4. Add convection

The wintertime convection may play an important role in the intensification and the maintenance of anticyclonic eddies (Gelderloos et al., 2011; Bosse et al., 2016, 2019), in particular in high latitude areas such as the RT. To discuss the impact of the convection on the intensity of the RT eddy, we ran simulations with a surface net heat flux (SNHF) representative of the RT area. It is calculated as an average of the SNHF (from Carton et al., 2018) in the area of latitude and longitude comprised respectively between  $53^\circ\text{N}$  and  $57^\circ\text{N}$ , and  $15^\circ\text{W}$  and  $11^\circ\text{W}$ . The annual variation of SNHF imposed in the simulations with convection is shown in Fig. 4.

### 2.1.5. Sum up

A total of 16 simulations have been run and analyzed, to study the impact of the different parameters (presence and depth of the SCV

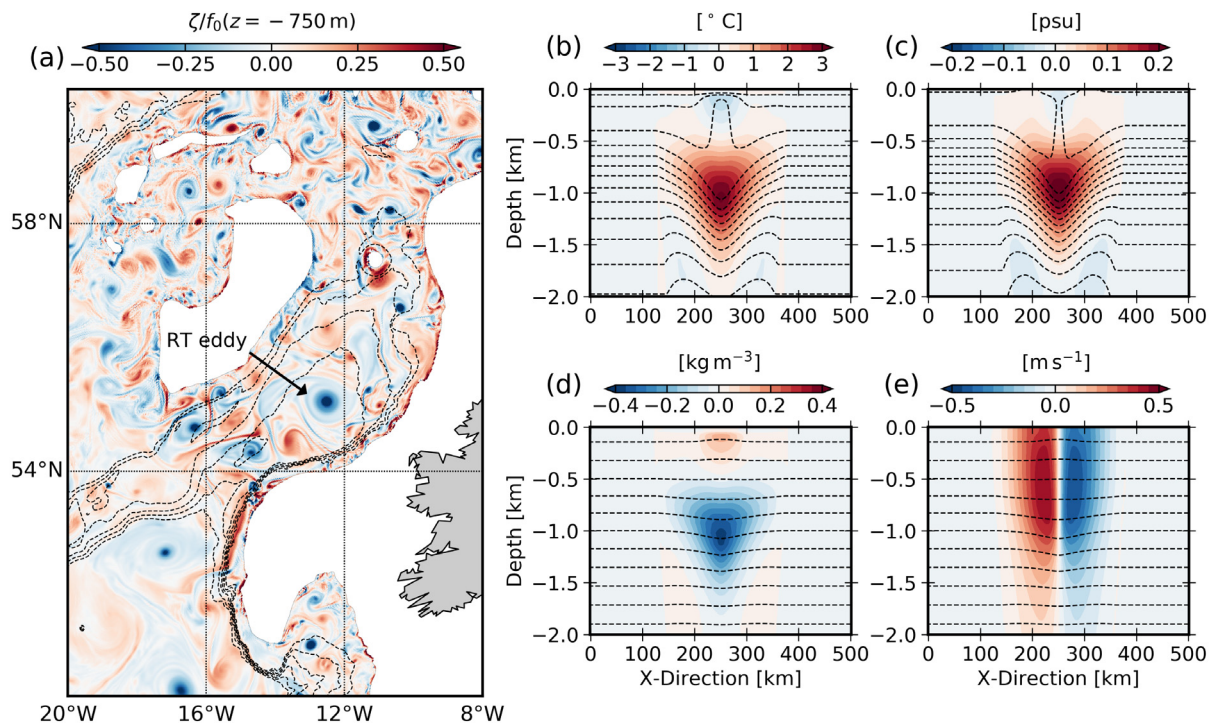


**Fig. 3.** (a) Snapshot of normalized relative vorticity at 750 m depth in the Rockall Trough area, from the realistic simulation (Le Corre et al., 2020) in which the composite anticyclone was extracted; dashed contours show isobaths from 3500 to 2000 m depth with a 250 m interval. (b,c,d,e) Temperature anomaly, salinity anomaly, density anomaly, and azimuthal velocity of the composite anticyclone; dashed contours show isolines of temperature (b), salinity (c), and density (d,e).

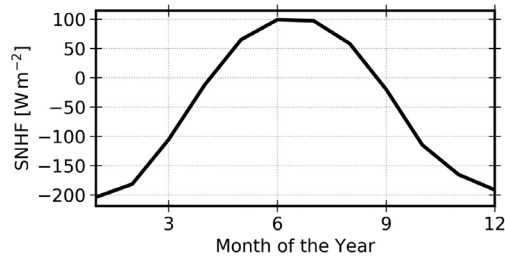


**Fig. 4.** Surface net heat flux imposed in idealized simulations with convection.

shotgun, presence of the RT eddy at initialization, convection, bottom drag) on the RT eddy intensity and dynamics. The different simulations are summarized in Table 1.

mRTDC is the simulation closest to the reality, as it includes all features and forcings occurring in the RT area: SCVs generated at a realistic depth, convection, bottom drag, and a anticyclonic eddy at the center of the bowl-like topography.

## 2.2. Diagnostics

We describe in this section the diagnostics performed on the simulation outputs.

### 2.2.1. Detection of the main eddy

In each simulation, we detect the main eddy using the Angular Momentum Eddy Detection and tracking Algorithm (AMEDA, Le Vu et al., 2018). One of the benefits of AMEDA is that it does not depend on arbitrary thresholding, which would require a fine-tuning of geometrical parameters. Also, the algorithm is robust with respect to the grid resolution and can thus be applied to a wide variety of velocity fields (experimental, numerical, derived from altimetry). This algorithm has been used and validated in previous – observational and numerical –

studies (Ioannou et al., 2017; Le Vu et al., 2018; Garreau et al., 2018; de Marez et al., 2019; de Marez et al., 2020), see also an example of application of AMEDA in <https://www1.lmd.polytechnique.fr/dyned/>. This algorithm works as follows: (a) from the velocity fields, it computes the local normalized angular momentum (LNAM, Mkhinini et al., 2014) and the local Okubo–Weiss parameter (LOW) at each point; (b) then, it seeks LNAM local maxima where  $\text{LOW} < 0$ ; (c) if these maxima are surrounded by a closed streamline, they are flagged as eddy centers. A full description of the algorithm is presented in Fig. 1 of Le Vu et al. (2018). In this study, the detection is done using daily velocity fields, at -250, -500, -750, -1000, and -1250 m depth for surf, middle surf, middle, middle deep, and deep cases respectively. Choosing the depth of detection as equal to the depth of SCV generation ensures an accurate estimation of the radius increase of the main eddy when it merges with SCVs. The main eddy's edge is defined as its contour of maximal velocity. The mean radius of this contour at a given time is  $R_{\max}$ . We use this contour to compute volume integrated quantities, assuming that the eddy is roughly cylindrical.

In simulations with a composite anticyclonic eddy at initialization, the main eddy is simply the initial eddy, that we follow in time. For simulations with no eddy at  $t=0$ , the main eddy is defined as the first SCV that reaches the center of the bowl-like topography and then grows in size due to merging with other SCVs.

### 2.2.2. Kinetic energy budget

In the primitive equation framework, the kinetic energy (KE) equation can be obtained by taking the inner product of the horizontal velocities with the momentum equations. It follows:

$$\frac{1}{2} \partial_t u_i^2 + u_j \partial_j \left( \frac{1}{2} u_i^2 \right) + u \partial_z \left( \frac{1}{2} u_i^2 \right) = \frac{u_i}{\rho_0} \partial_i P + \mathcal{V}_i u_i + D_i u_i + S_i u_i, \quad (1)$$

with summation convention,  $i = 1, 2$ , and  $j = 1, 2$ ,  $u_i$  are the horizontal component of velocity,  $\partial_i$  the components of the vector differential operator,  $\mathcal{V}_i$  the components of the parameterized vertical mixing,  $D_i$  the components of the horizontal diffusion, and  $S_i$  other sources and sinks (due to restoring, nudging, boundary conditions...). This equation is then vertically integrated, and we define:

**Table 1**  
Parameters of the analyzed simulations.

Name	SCV shotgun	RT eddy at initialization	Bottom drag	Convection
dD	deep	–	yes	–
mD	middle	–	yes	–
m	middle	–	–	–
sD	surf	–	yes	–
RTD	–	yes	yes	–
RT	–	yes	–	–
RTDC	–	yes	yes	yes
dRTD	deep	yes	yes	–
dRTDC	deep	yes	yes	yes
mdRTD	middle deep	yes	yes	–
mRTD	middle	yes	yes	–
mRT	middle	yes	–	–
mRTDC	middle	yes	yes	yes
msRTD	middle surf	yes	yes	–
sRTD	surf	yes	yes	–
DC	–	–	yes	yes

- $\text{hadv} = \int dz u_j \partial_j (\frac{1}{2} u_i^2)$ ,
- $\text{vadv} = \int dz w \partial_z (\frac{1}{2} u_i^2)$ ,
- $\text{Prsgrd} = \int dz \frac{u_i}{\rho_0} \partial_i P$ ,
- $\text{vmix} = \int dz \mathcal{V}_i u_i$ ,
- $\text{hmix} = \text{explicit part of } \int dz D_i u_i$ ,
- $\text{hdif} = \text{implicit part of } \int dz D_i u_i$ ,
- $\text{nudg} = \int dz S_i u_i$ ,
- $\text{cor} = \int dz (fuv - fvu)$ ,
- $\text{vol}$  = the depth integrated KE variations due to the grid breezing,
- Drag = contribution of the bottom drag parameterization in the vmix term.

All these terms are computed online (Gula et al., 2016). The closed KE budget is:

$$\partial_t \int dz \frac{1}{2} u_i^2 = \text{hadv} + \text{vadv} + \text{Prsgrd} + \text{vmix} + \text{hmix} + \text{hdif} + \text{nudg} + \text{cor} + \text{vol}. \quad (2)$$

We integrate these terms in time, such that for instance  $\int_0^t dt$  Drag represents the contribution of the bottom drag for the KE at a given time  $t$ . Finally, we horizontally integrate the results in the main eddy's contour  $S$  (calculated by AMEDA). This allows to follow in detail which physical mechanism is responsible for the evolution of the main eddy's KE.

### 3. Results

In this section, we describe the results of our study. We first explain qualitatively the course of a simulation representative of the RT, i.e., the mRTD simulation. Then we discuss the impact of the different parameters on the evolution of the main eddy.

#### 3.1. Qualitative evolution of the simulations

In the mRTD simulation, the main eddy is present from  $t = 0$  at the center of the bowl topography (see Fig. 5 for the time evolution of the mRTD simulation). Because it is anticyclonic, it is stuck in the center of the bowl to conserve its potential vorticity (Carnevale et al., 1991). Thus, it cannot climb out without external disturbance. During the first year of the simulation, the main eddy does not move from the center of the bowl. Its volume slightly increases because of a azimuthal mode 2 and mode 4 destabilization, similar to the one observed in de Marez et al. (2020a) (a vorticity tripole can be seen at  $t = 5$  months in Fig. 5).

Simultaneously, SCVs are generated at the corner of the land mask. As shown in Deremble et al. (2016), such boundary singularities generate dipolar structures. In our case, about 35 dipoles are generated each

year. The anticyclonic pole is attracted by the bowl, while the cyclonic pole tends to step aside. Indeed, on a slope, the topographic  $\beta$ -drift makes anticyclones (resp. cyclones) drift downhill (resp. uphill) (La-Casce, 1998; Lam and Dritschel, 2001). This leads to the separation of about all dipoles in two monopoles of opposite vorticities. Also, in some cases, the positive pole is rolled up around the anticyclone, leading to a shielded anticyclonic SCV. In both cases, this results into anticyclonic SCVs attracted by the bowl. However, they do not all reach the bowl (i.e., the places where the floor is deeper than 2000 m): only about ten anticyclonic SCVs per year manage to reach it. This is mainly due to the fact that just after generation, SCVs merge between each other, and subsequently converge to the center of the bowl.

At the start of the second year of simulation, SCVs start to interact with the main eddy. These SCVs have two effects.

First, the SCVs' velocity field slightly disturb the main eddy, resulting in small displacements of the main eddy in the bowl. From this date, the main eddy can thus be found at tens of kilometers from the center of the bowl, see e.g.  $t = 15, 25$ , or 55 months, in Fig. 5.

Second, SCVs merge with the main eddy. In this simulation – i.e., during about 7 years and a half – 41 merging events between SCVs and the main eddy are observed. Two kinds of merger occur. On the one hand, small SCVs that have experienced a few merging with other SCVs before reaching the bowl, are attracted by the main eddy and steered around it. They are finally absorbed by the main eddy which eventually grows by aggregating vorticity and azimuthal velocity outside of its core (Sutyrin and Radko, 2019; Sutyrin, 2019). This mechanism is referred to as *Vortex Thinning* in the literature. A vortex thinning event results in a small increase of the eddy volume; examples can be seen at  $t = 15$  or 70 months in Fig. 5. On the other hand, the main eddy can merge with SCVs that have grown in size due to successive merging with other SCVs. This results in situations where the main eddy is either of the same size of the vortex it merges with, or smaller than it. In both cases, the merging is roughly symmetric, and it results in an abrupt increase of volume of the main eddy. An example can be seen between  $t = 30$  and 35 months in Fig. 5.

These mergers can also be called alignment, because the main eddy's core density is not necessarily the same than its companion's one (see e.g. Nof and Dewar (1994), and sections 7.1.3 and 7.2.4 of Lilly et al. (2003) that discuss cases of vortex alignment in the Labrador Sea). It can be mentioned that, in a stratified fluid, mergers must manifest as alignment because there will always be small differences in the core density of the two eddies. The impact of this three-dimensional view is discussed in the next sections. Also, we detail in the following the physical mechanism that occur in the simulations, and lead to changes of volume for the main eddy.

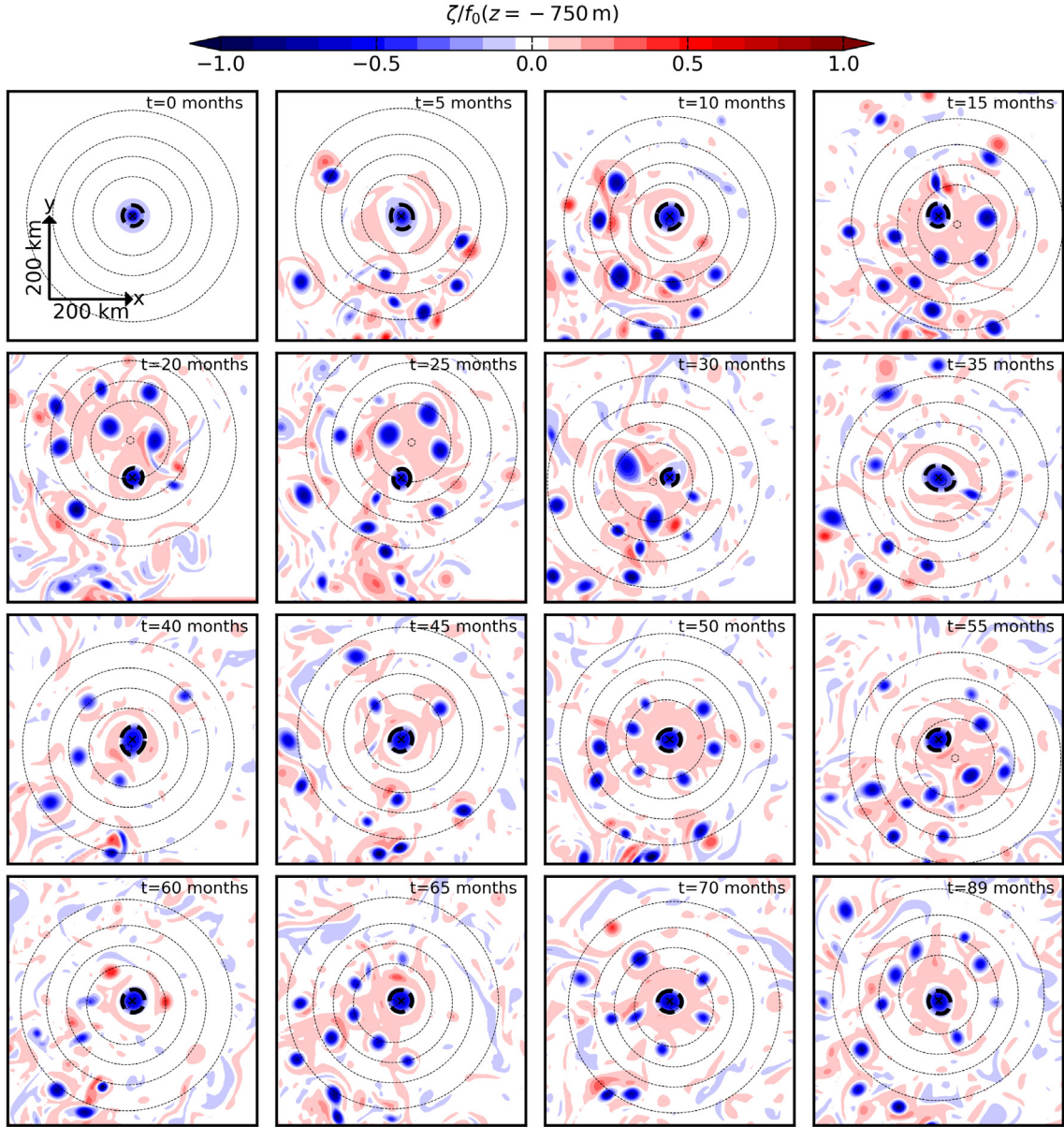


**Fig. 5.** Snapshots of normalized relative vorticity at 750 m depth, in the mRTD simulation. Each panel is 600 km large, and is centered around the main eddy. Bold dashed contours indicate the contour of maximum velocity of the main eddy. Thin dashed contours show isobath from 2500 to 2000 m depth with a 100 m interval.

### 3.2. Mechanisms of eddy growth

In all simulations, as in e.g., mRTD (see Fig. 5), the main eddy growth is intermittent and occurs at specific moments of the simulation. As discussed in the introduction, this eddy growth can be attributed to two mechanisms: merging with vortex companions, and convection. We detail in this section these physical mechanisms.

#### 3.2.1. Merging with SCVs

To discuss the impact of merger on the main eddy, we analyze the time evolution of  $R_{\max}$  in different simulations, see Fig. 6. Both kinds of merging events discussed in the previous section for mRTD simulation – vortex thinning and symmetric merger – can be seen in Fig. 6(a). They appear as steps in the time evolution of  $R_{\max}$ , at e.g.,  $t = 35$  or  $75$  months (in the mRTD simulation, see arrows in Fig. 6(a)). In all simulations, symmetric mergers have a greater impact on  $R_{\max}$ , as it can double the radius of the main eddy in a few days.

In all simulations with the RT composite at initialization (Fig. 6(a)), the radius of the main eddy oscillates around about 30 km. After

periods of radius decrease, the merging efficiently increases the radius. The horizontal extension of the main eddy is thus similar to its initial one after 7 years of simulation. It can be noticed that in the sRTD simulation, the main eddy appears to have a larger radius than in other simulations. Even with this difference, the purely horizontal view described by the time evolution of  $R_{\max}$  is qualitatively similar in dRTD, mdRTD, mRTD, msRTD, and sRTD.

The main difference between the simulations is the final vertical shape of the main eddy, e.g., after 66 months (Fig. 7). In the dRTD simulation, the main eddy has a 3D shape similar to the initial RT composite. This is due to the fact that SCVs have difficulty to merge with the main eddy. Oppositely, in the sRTD and msRTD simulations, SCVs easily merge with the main eddy, and thus drastically modify its 3D shape. The final shape of the main eddy differs from the RT composite because it is intensified at the surface, with a larger horizontal extension due to the numerous mergers it experienced. In the mRTD and mdRTD simulations, the merging events lead to an important intensification of the eddy intensity at depth. In the mdRTD simulation, the final shape

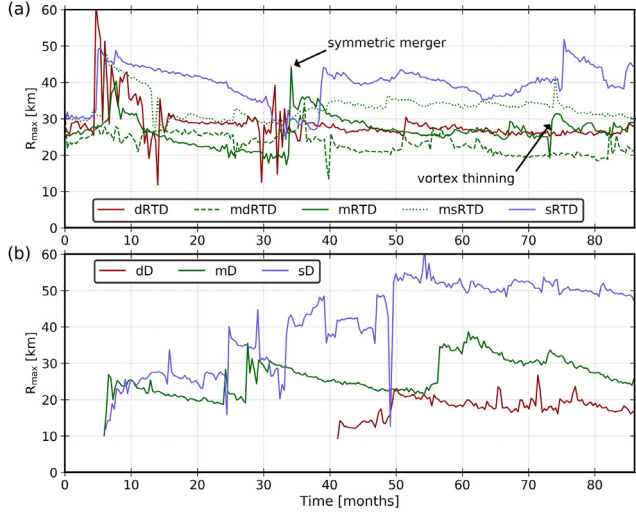


**Fig. 6.** Evolution of  $R_{\max}$  during simulations, for different initialization depth of the SCV shotgun (a) with and (b) without the RT composite at the center of the bowl. All simulations include bottom drag parameterization.

of the main eddy is a double-core eddy, with two vorticity maxima, at ~500 m depth and ~1300 m depth.

The merging efficiency is not the same in all simulations because of (1) the background stratification, and (2) the vertical structures of the main eddy and the SCVs it merges with. Indeed, Verron et al. (1990), Verron and Valcke (1994), Corréard and Carton (1999) altogether showed, using 2-layer numerical simulations, that the merger (or alignment) of two like-signed vortices depends on their shape before the merging. Vortices can be separated into two kinds: PVI (potential vorticity initialization) vortices and RVI (relative vorticity initialization) vortices. PVI vortices are represented by a patch of constant potential vorticity in a single layer – and in some cases a vertical dipole of potential vorticity –, associated with nearly barotropic

relative vorticity. RVI vortices have a constant relative vorticity in a single layer. Corréard and Carton (1999) showed that PVI vortices easily align together while RVI vortices do not. Verron et al. (1990), Verron and Valcke (1994) showed that the ambient stratification plays a different role in the merging depending on the vortex shape: RVI vortex merger strongly depends on the stratification while PVI vortex merger does not. If the stratification is weak, RVI vortices form a pair of heton-like structures, that repel each other. If the stratification is stronger, the ambient flow is more barotropic, and merger is easier. In a configuration more realistic than the 2-layer quasi-geostrophic model, like in our study, the distinction between RVI or PVI vortices can be tricky because of the Gaussian vertical shape that eddies often take (McWilliams, 1985).

In our simulations, the categorization of eddies is difficult because the main eddy and its companion eddies can be categorized as PVI-like vortices (they appear as – roughly constant – PV patches confined in a single layer, see Fig. 8), but also RVI-like vortices (the maximum of relative vorticity is confined in ~1000 m deep layers, around which the relative vorticity either changes sign or is close to zero). Merging vortices are thus PVI/RVI hybrids. The background stratification should thus play a role in the merger efficiency. Our background stratification is similar to the RT case (Fig. 1(d)) and it has Brunt–Väisälä frequency maxima at the surface and near 750 m depth. Thus for RVI vortices, the merger is facilitated at these particular depths, while it is harder to merge for deeper eddies. This could explain in part why SCVs have more difficulties to merge with the main eddy in the dRTD simulation than in the other simulations.

One can observe a critical depth for the SCV shotgun, between 1000 and 750 m depth, for which the merging/alignment of eddies do not lead to the intensification of the main eddy's core. If SCVs are close enough (in both vertical and horizontal directions), they eventually align with the main eddy, but this only results in a deepening of the eddy and/or a double-core eddy, with no influence on the original eddy core. Because of the complicated form of eddies and ambient stratification, it is here difficult to be more quantitative about the key parameters that influence the merging. A more extensive study in the parameter space would be necessary to discuss in details the alignment of vortices in a 3D primitive equation framework.

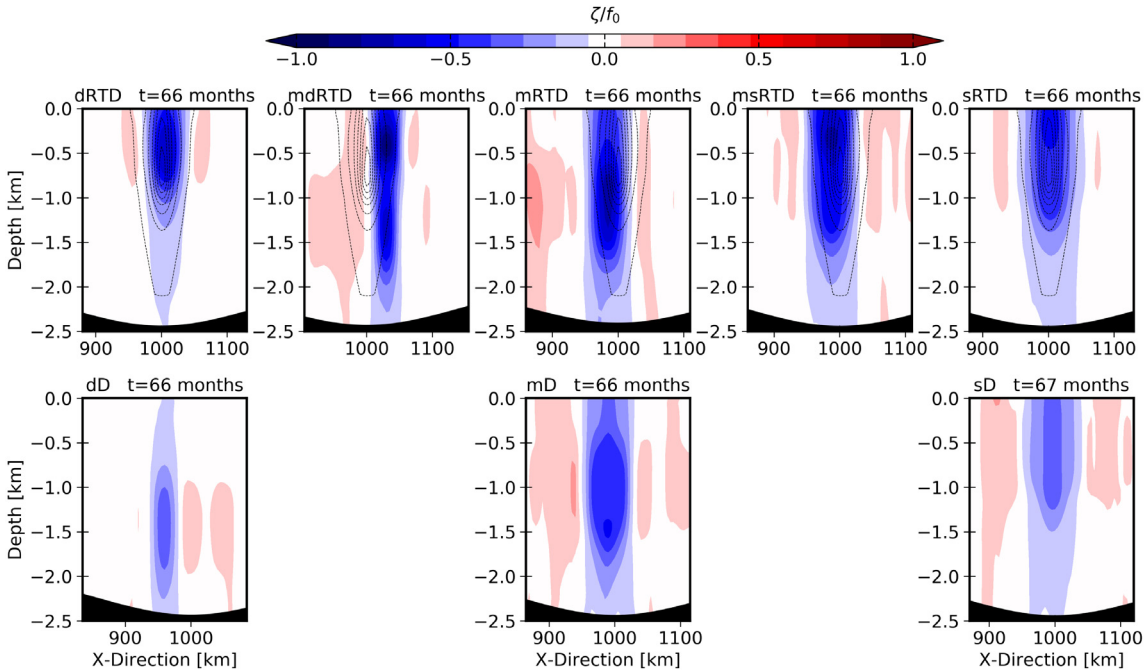


**Fig. 7.** Vertical sections of normalized relative vorticity passing through the center of the main eddy after ~5 and a half years of simulation, for simulations shown in Fig. 6. Thin contours in the top row show the contours of normalized vorticity through the center of the RT composite at initialization; note that line and color contours are shown for the same vorticity values.

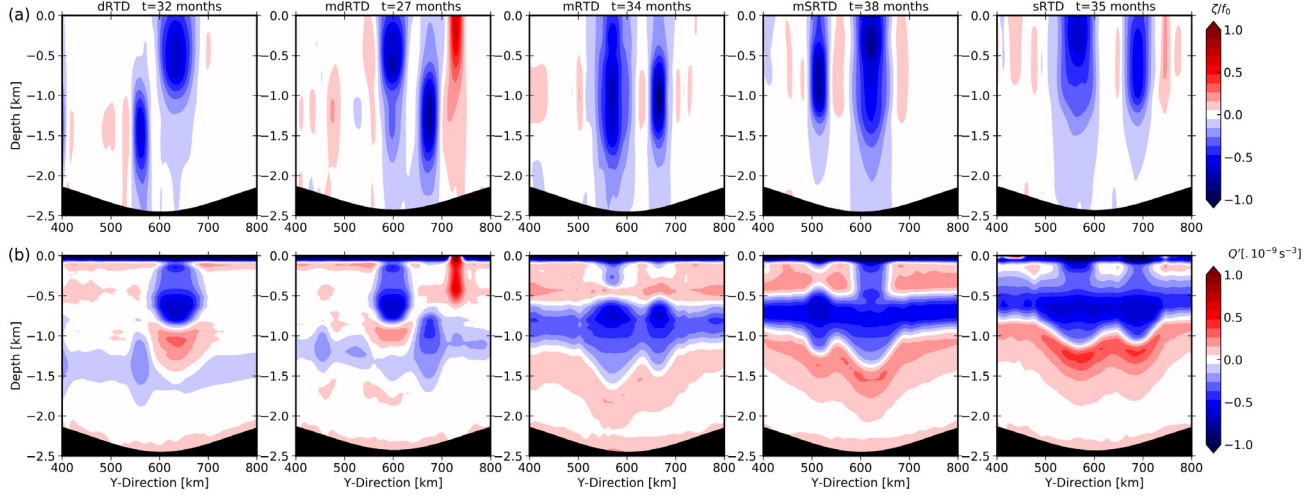


**Fig. 8.** Vertical section of (a) normalized relative vorticity and (b) associated PV anomaly, at times just before a merger of the main eddy with a companion eddy, in dRTD, mdRTD, msRTD, and sRTD simulations. All sections pass through the center of both eddies.

If no initial RT composite is present, the time evolution of  $R_{\max}$  (Fig. 6(b)) is roughly similar to cases described above. However, the main eddy vertical structure near the end of the simulation is strongly influenced by the SCVs generation depth (Fig. 7). In the dD simulation, SCVs hardly merge, because of the weak stratification below 1000 m depth, leading to a weak resulting eddy, intensified at depth. In the sD simulation, SCVs are not very intense, but they easily merge, leading to a weak surface-intensified anticyclone, that does not resemble the RT eddy either. In the mD simulation, the final shape of the main eddy is roughly similar to the mRTD simulation's one. This shows that the merging of SCVs between each other produces an eddy similar to the RT eddy only if SCVs are generated at a realistic depth, where merger is easier because of the strong stratification. This supports the view of Smilenova et al. (2020), that from an ocean at rest, the RT eddy results from a succession of merging events between SCVs generated at ~750 m depth.

### 3.3. On the importance of convection

If we add a negative heat flux at the surface (as in RTDC, mRTDC or DC simulations), convection appears. As a result, isopycnals deepen during about 6 months each year, following the imposed seasonal cycle (Fig. 4). The Ertel potential vorticity  $Q$  defined as

$$Q = (f_0 + \zeta) \partial_z b - (\partial_z v)(\partial_x b) + (\partial_z u)(\partial_y b), \quad (3)$$

with  $f_0$  the Coriolis frequency,  $b$  the buoyancy, and  $\zeta$  the relative vorticity, undergoes a seasonal increase in the main eddy's core (see Fig. 9(b)). The shallower the SCV shotgun is, the larger this intensification. This mechanism of intensification by wintertime convection is rather multifaceted. The deepening of the core intensifies radial density gradients and subsequently increases the azimuthal velocity of the eddy. During these convective periods the main eddy is thus intensified, and its radius increases (see Fig. 9(a)). On the other hand, when density gradients are increased the eddy is no longer in thermal wind balance, and therefore an adjustment mediated by a secondary circulation is required. We refer the reader to Legg et al. (1998), Legg and McWilliams (2001) for a full explanation of this process.

If we compare the RTD and the RTDC simulations, one can see that even if no SCV shotgun is present, the evolution of the main eddy's radius experiences sharp increases in the presence of convection. This is due to the fact that during convective periods, the surface mixed-layer deepens in the whole domain, and SCVs are spontaneously generated by mixed-layer baroclinic instabilities (Callies et al., 2015). This leads

to vortex thinning events between convectively-generated SCVs and the main eddy, that subsequently increase the main eddy's radius (Schubert et al., 2020). These events appear throughout the whole simulation involving convection, and they are difficult to characterize because they can be generated above the main eddy and merge with it within a few days. However, it can be noticed that in the simulation with both a SCV shotgun at mid-depth and convection (mRTDC), we observe that the main eddy's radius continuously oscillates between a mean value of about 30 km. In this simulation, the SCVs are more numerous than in the mRTD simulation. The number of merging events of small SCVs with the main eddy is larger when convection is present. This leads to a lot of small increases of radius rather than decrease periods followed by a large increase.

Convection and merging events with convectively-generated SCVs act together to increase the horizontal shape of the main eddy, but also its intensity at depth. Indeed, with convection, the main eddy is more intensified at depth than in simulation without convection, see e.g., Fig. 9(c) for the dRTDC simulation. The main eddy is intensified at a depth where no merging with neither the convectively-generated SCVs in the mixed-layer nor the SCV shotgun SCVs occurs. This reflects the importance of the direct convectively driven mode. As mentioned in the previous section, if the SCVs are generated below a critical depth (e.g. in dRTD simulation), little merging events are observed. If we add the convection (dRTDC simulation), the main eddy's core deepens. Subsequently, the vertical distance between the main eddy's core and SCVs decreases, and merger/alignment is eased. This leads to a deep intensification of the main eddy, see Fig. 9(c). Convection thus allows to intensify the main eddy's core by (1) deepening the core during wintertime, (2) generating small SCVs – by mixed-layer instabilities – that can eventually merge with the main eddy, and (3) helping alignment by reducing the distance between the main eddy's core and deeply-generated SCVs. It should be noticed however that from our analysis, the relative importance of these three mechanisms cannot be precisely gauged. This quantification should be the aim of further investigations.

As a sensitivity test, we also ran a simulation with only convection (DC simulation, not shown). In this simulation, anticyclonic convectively-generated SCVs are attracted by the bowl-shaped topography. They subsequently merge between each other, and eventually form a ~50 km radius anticyclone in the bowl, i.e., a main eddy. This eddy appears after about 33 months of simulation and is intensified between 1000 and 1500 m depth. This test further shows that the convection by

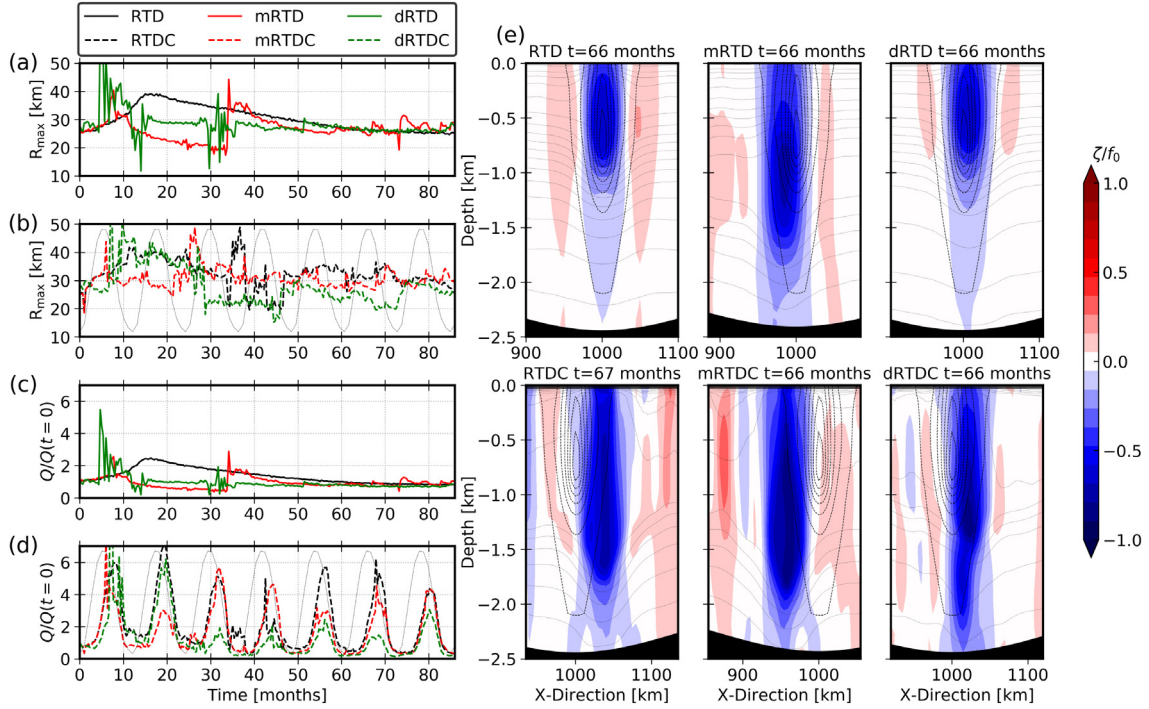


**Fig. 9.** (a,b) (resp. (c,d)) Time evolution of  $R_{\max}$  (resp. ratio between PV and initial PV integrated over the main eddy) for some simulations without (a,c, solid line) or with (b,d, dashed lines) convection; the thin gray line shows the time evolution of the SNHF applied at the surface in the simulations with convection (see Fig. 4 for the values it reaches). (e) Same as Fig. 7 for the 6 simulations shown in (a,b).

itself is sufficient to lead to a single long-lived anticyclonic eddy in a bowl topography.

#### 3.4. Mechanisms of eddy decay

As can be seen in the time evolution of  $R_{\max}$  (see e.g., Fig. 6), after the main eddy's radius increases due to either merging or convection, periods of decay that can last for several years are observed. During these periods, little merging occurs, and some physical mechanisms lead to the erosion of the eddy. We describe those in the following section.

##### 3.4.1. Bottom drag

The principal mechanism responsible for the eddy decay in our simulations is the bottom drag. We observe that no radius decay period are seen in simulations without bottom drag parameterization (Fig. 10(a)). This leads to a main eddy being too intense, and too large in comparison with the RT eddy. Also, without drag, the main eddy becomes anomalously barotropic (see for instance Fig. 11(c)). It thus has a 3D shape very different from the RT eddy.

The bottom drag seems to be the major limiting factor for the eddy growth due to merging with SCVs. In the KE equation budget (Fig. 10(b)) the pressure gradient, the advection and the Coriolis terms dominate the main eddy's KE gain (C in Fig. 10(b)). They are the result of merging with other coherent structures (SCVs), and conversion from potential to kinetic energy (not shown). The horizontal diffusion and mixing, as well as volume change and nudging have a neglectable contribution to the KE budget (B). The bottom drag ( $A_1$ ), included in the vertical mixing ( $A_2$ ), appears to dominate the main eddy's KE loss. It compensates the other terms, and increases in amplitude each time the eddy gains KE by merging with other vortices. The bottom drag contribution is intensified when the main eddy drifts away from the center of the bowl, because the water depth is smaller. It is thus greater just before symmetric merger events, because the main eddy co-rotates with its companion, and subsequently drifts away from the center of the bowl. This can be seen in Fig. 10(b), with Drag KE term peaking just before merging related steps (see at e.g.  $t = 35$  months).

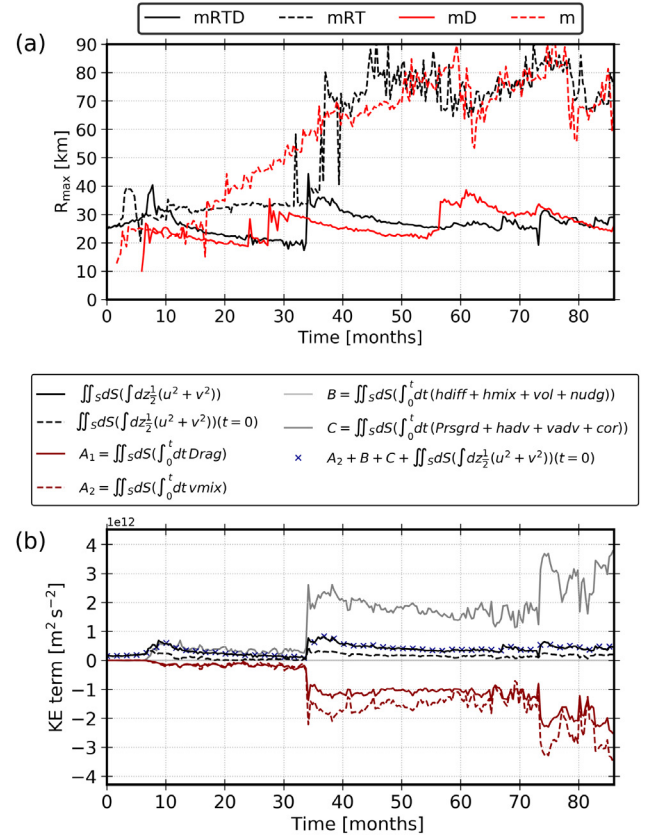


**Fig. 10.** (a) Evolution of  $R_{\max}$  during simulations, with (solid) and without (dashed) bottom drag parameterization. (b) Evolution of kinetic energy terms in the mRTD simulation. Each term is integrated in time and in the contour of the main eddy. Note that the superposition of blue crosses with the black solid lines shows that the KE energy budget is closed, with respect to Eq. (2).

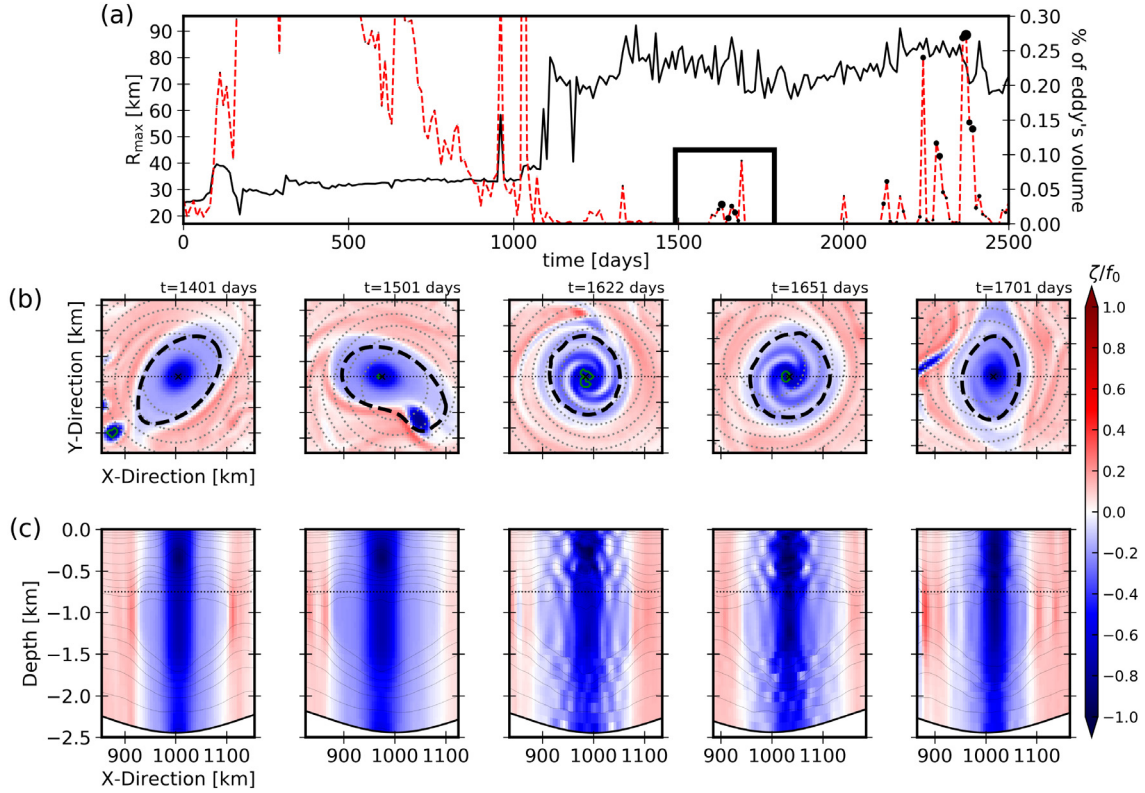


**Fig. 11.** (a) Time evolution of  $R_{\max}$  (black line) and % of eddy's volume with negative PV (dashed red) for the mRT simulation. The size of black dots indicates the amplitude (in absolute value) of the minimum PV in the eddy's contour. (b) Horizontal sections of normalized relative vorticity at 750 m depth; green contours indicate the places where the PV is negative. (c) Vertical sections of normalized relative vorticity passing through the center of the main eddy; the thin dashed lines indicate the depth of horizontal sections shown in (b).

#### 3.4.2. Centrifugal instability

In cases without drag, it can be seen that the main eddy still experiences abrupt radius decrease events, see e.g., between  $t = 1500$  and 1700 days in mRT simulation (Fig. 11(a)). At this time, a rapid radius decrease is seen just after a vortex thinning event with a small SCV. Horizontal sections of relative vorticity (Fig. 11(b)) show that after the main eddy absorbs the SCV, a spiral-like pattern appears in the eddy's core. This pattern is seen in the whole water column. There, the normalized relative vorticity reaches  $\zeta/f_0 \sim -1$ .

This pattern is typical of centrifugal instability (Cushman-Roisin and Beckers, 2011). This diagnostic is confirmed by the following facts. (1) The PV in the eddy's core is negative near its center (green contours in Fig. 11(b)), which is the necessary condition ( $fQ < 0$ ) for centrifugal instability. (2) The horizontal shear terms are responsible for the extreme decrease of PV in the eddy's core (not shown).

Negative PV patches are strongly unstable, and the nearly materially conserved nature of PV implies that negative PV does not occur spontaneously inside the fluid. Thus, the generation of negative PV in the fluid must be forced, for instance by appropriate frictional interactions with nearby boundaries or interactions with the wind. Here, no such mechanism is present. The decrease of PV is due to the abrupt change of horizontal velocity gradients resulting from the vortex thinning of a small SCV around the main eddy (Fig. 11(b)). The change of PV occurs where density fronts are sharp and parameterized diapycnal mixing occurs (see Appendix C in de Marez et al. (2020a)). The centrifugal instability is thus triggered by the interaction of the main eddy with the SCV, and eventually leads to an abrupt erosion of the eddy. About five major centrifugal instability events occur at  $t > 1000$  days, see the peaks of red dashed curve in Fig. 11(a), that show times when negative PV is seen in the eddy's core. Note that before  $t = 1000$  days, negative PV is found in the eddy's core, but with values very close to zero. The eddy is thus at this moment not intense enough to be subject to the instability.

Such centrifugal instabilities are preferably seen in simulations without drag. In those, the main eddy is more intense, and it reaches very low PV values that are suitable for instabilities. Nevertheless, such instabilities can still be seen in e.g., mRTD simulation, with a smaller signature than in mRT (not shown).

#### 4. Summary and discussion

We studied the lifecycle of an anticyclonic eddy trapped in a bowl-like topography, which is subject to the interaction with like-signed SCVs and/or convection. From the analysis of 16 simulations with varying parameters, we show that the balance between merger and bottom drag allows the eddy to have a roughly constant 3D shape throughout several years. On the one hand the vortex merger with small SCVs allows the eddy to grow in size, and intensify at depth. As merger events occur at the SCV generation depth, the final main eddy is intensified at this particular depth. These mergers are enhanced when SCVs are generated at a depth where the stratification is large, and when convection is at work. Indeed, the convection (1) deepens the main eddy and increases the merger efficiency at depth, and (2) generates other SCVs in the mixed-layer that eventually merge with the main eddy. On the other hand the bottom drag erodes the eddy. The bottom drag is the main contribution to the eddy's KE loss. When it is not included in simulation, the eddy becomes barotropic, and centrifugal instabilities triggered by the merger with SCVs erode the eddy over the whole water column.

Merging and convection both contribute to the maintaining of anticyclonic eddies trapped in bowl-shaped topographies. Our study thus shows that it is difficult to disentangle the two mechanisms, in particular if we replace this in a more realistic context. However, the final shape of the main eddy can give keys about the mechanisms responsible for the long lifetime of such eddies. If the main eddy is intensified at

multiple depth (it has e.g., a double-core eddy), the eddy has certainly experienced one or several merging with other vortices. Also, if the depth of intensification of the main eddy is correlated with the depth of a SCV generation site nearby, merger between these vortices probably happened. One can therefore state that in these cases, merging played a major role in the maintaining of the eddy.

In the real ocean, other processes can affect the shape of such an eddy. For instance, internal waves and fine-scale ( $\mathcal{O}(1)$  m) processes can lead to the dissipation of long-lived mesoscale eddies. In the LV case, Fer et al. (2018) showed through high-resolution turbulence measurements that the background shear as well as near-inertial waves trapped by the negative vorticity of the LV are the dominant sources of kinetic energy loss. More generally, internal waves are suspected to drain a significant part of the energy of such mesoscale eddies (Barkan et al., 2021). These mechanisms are hardly resolved in the simulations discussed in the present paper, and are mainly controlled by the numerical parameterization (i.e., the vertical mixing induced by the KPP scheme). Furthermore, the simulation lacks realistic levels of internal waves. Simulations with higher resolution and fully realistic atmospheric and tidal forcings should thus be required in order to determine the relative importance of these other processes compared to the bottom drag. At larger scales opposite-signed mesoscale coherent structures can travel to the eddy's location. This could modify the behavior of the eddy by dipolar effect, and affect the merging efficiency with SCVs (Rodríguez-Marroyo et al., 2011). Furthermore, the presence of a mean current due to large-scale circulation or local coastal current can erode the eddy because of the presence of an ambient horizontal shear (Perrot and Carton, 2010). If the eddy moves toward the coast, the interaction with coastal Kelvin waves can also affect its trajectory and shape (Dewar and Hogg, 2010; Gula and Zeitlin, 2010; Hogg et al., 2011; de Marez et al., 2020b).

Despite this, in the Rockall Trough (as well as in e.g., the Lofoten Basin) the semi-permanent anticyclonic eddies are rather isolated from the coast and other currents. Our study can thus support the view of Smilenova et al. (2020) or Trodahl et al. (2020) that such semi-permanent anticyclonic eddies are mainly maintained by the merger (or alignment) with smaller-scale vortices. In this high latitude regions, convection is large, and indeed deepens isopycnal and subsequently increases the eddy's core potential vorticity, as discussed in e.g., Bosse et al. (2019). However, we show here that convection principally enhances the number of merger with small eddies, either at the surface or at depth with SCVs. The merging/alignment with SCVs is thus likely to be the more important mechanism to sustain mesoscale anticyclones trapped in a bowl, as stated in the LV case by Trodahl et al. (2020) and by Smilenova et al. (2020) in the RT eddy case.

#### CRediT authorship contribution statement

**Charly de Marez:** Conceptualization, Methodology, Software, Writing – original draft. **Mathieu Le Corre:** Software, Writing – review & editing. **Jonathan Gula:** Writing – review & editing, Supervision, Funding acquisition.

#### Declaration of competing interest

The authors declare that they have no known competing financial interests or personal relationships that could have appeared to influence the work reported in this paper.

#### Acknowledgments

This work was funded by the Direction Générale de l'Armement (DGA), France via a full grant for Charly de Marez's Ph.D. J.G. gratefully acknowledges support from the French National Agency for Research (ANR) through the project DEEPER (ANR-19-CE01-0002-01). Simulations were performed using the HPC facilities DATARMOR of 'Pôle de Calcul Intensif pour la Mer' at Ifremer, Brest, France. The authors thank X. Carton for helpful discussions.

#### References

- Barkan, R., Srinivasan, K., Yang, L., McWilliams, J.C., Gula, J., Vic, C., 2021. Oceanic mesoscale eddy depletion catalyzed by internal waves. *Earth Space Sci Open Archive* 14. <http://dx.doi.org/10.1002/essoar.10507068.1>.
- Bosse, A., Fer, I., Lilly, J.M., Soiland, H., 2019. Dynamical controls on the longevity of a non-linear vortex : The case of the Lofoten Basin Eddy. *Sci. Rep.* 9, <http://dx.doi.org/10.1038/s41598-019-49599-8>.
- Bosse, A., Testor, P., Houpert, L.C., Damien, P., Prieur, L., Hayes, D., Taillandier, V., Durrieu de Madron, X., d'Ortenzio, F., Coppola, L., Karsten, J., Mortier, L., 2016. Scales and dynamics of submesoscale coherent vortices formed by deep convection in the northwestern Mediterranean Sea: Vortices in the NW Mediterranean Sea. *J. Geophys. Res. Oceans* 121, 7716–7742. <http://dx.doi.org/10.1002/2016JC012144>.
- Callies, J., Ferrari, R., Klymak, J.M., Gula, J., 2015. Seasonality in submesoscale turbulence. *Nature Commun.* 6, <http://dx.doi.org/10.1038/ncomms7862>.
- Carnevale, G., Kloosterziel, R., Van Heijst, G., 1991. Propagation of barotropic vortices over topography in a rotating tank. *J. Fluid Mech.* 233, 119–139. <http://dx.doi.org/10.1017/S0022112091000411>.
- Carton, J.A., Chepurin, G.A., Chen, L., Grodsky, S.A., 2018. Improved global net surface heat flux. *J. Geophys. Res. Oceans* 123, 3144–3163. <http://dx.doi.org/10.1002/2017JC013137>.
- Chelton, D., Gaube, P., Schlax, M., Early, J., Samelson, R., 2011. The influence of nonlinear mesoscale eddies on near-surface oceanic chlorophyll. *Science* 334, 6054. <http://dx.doi.org/10.1126/science.1208897>.
- Corréard, S.M., Carton, X., 1999. Vertical alignment of geostrophic vortices. In: IUTAM Symposium on Simulation and Identification of Organized Structures in Flows. Springer, pp. 191–200.
- Cushman-Roisin, B., Beckers, J.-M., 2011. *Introduction To Geophysical Fluid Dynamics: Physical and Numerical Aspects*. Academic Press.
- de Marez, C., Carton, X., L'Hégaret, P., Meunier, T., Stegner, A., Le Vu, B., Morvan, M., 2020. Oceanic vortex mergers are not isolated but influenced by the  $\beta$ -effect and surrounding eddies. *Sci. Rep.* 10, <http://dx.doi.org/10.1038/s41598-020-59800-y>.
- Deremble, B., Dewar, W.K., Chassignet, E.P., 2016. Vorticity dynamics near sharp topographic features. *J. Mar. Res.* 74, 249–276. <http://dx.doi.org/10.1357/002224016821744142>.
- Dewar, W.K., Hogg, A.M., 2010. Topographic inviscid dissipation of balanced flow. *Ocean Modell.* 32, 1–13. <http://dx.doi.org/10.1016/j.ocemod.2009.03.007>.
- Dong, C., McWilliams, J.C., Liu, Y., Chen, D., 2014. Global heat and salt transports by eddy movement. *Nature Commun.* 5, 3294. <http://dx.doi.org/10.1038/ncomms4294>.
- Fer, I., Bosse, A., Ferron, B., Bouruet-Aubertot, P., 2018. The dissipation of kinetic energy in the lofoten basin Eddy. *J. Phys. Oceanogr.* 48, 1299–1316. <http://dx.doi.org/10.1175/JPO-D-17-0244.1>.
- Garreau, P., Dumas, F., Louazel, S., Stegner, A., Le Vu, B., 2018. High-resolution observations and tracking of a dual-core anticyclonic Eddy in the Algerian basin. *J. Geophys. Res. Oceans* 123, 9320–9339. <http://dx.doi.org/10.1029/2017JC013667>, <http://doi.wiley.com/10.1029/2017JC013667>.
- Gelderloos, R., Katsman, C.A., Drijfhout, S.S., 2011. Assessing the roles of three Eddy types in restratifying the Labrador Sea after deep convection. *J. Phys. Oceanogr.* 41, 2102–2119. <http://dx.doi.org/10.1175/JPO-D-11-054.1>.
- Gula, J., Molemaker, J., McWilliams, J., 2015. Gulf stream dynamics along the Southeastern U.S. seaboard. *J. Phys. Oceanogr.* 45, 690–715. <http://dx.doi.org/10.1175/JPO-D-14-0154.1>.
- Gula, J., Molemaker, M.J., McWilliams, J.C., 2016. Topographic generation of submesoscale centrifugal instability and energy dissipation. *Nature Commun.* 7, <http://dx.doi.org/10.1038/ncomms12811>.
- Gula, J., Zeitlin, V., 2010. Instabilities of buoyancy-driven coastal currents and their nonlinear evolution in the two-layer rotating shallow-water model. Part 1. Passive lower layer. *J. Fluid Mech.* 659, 69–93. <http://dx.doi.org/10.1017/S0022112010002405>.
- Heywood, K.J., McDonagh, E.L., White, M.A., 1994. Eddy kinetic energy of the North Atlantic subpolar gyre from satellite altimetry. *J. Geophys. Res.* 99, 22525. <http://dx.doi.org/10.1029/94JC01740>.
- Hogg, A.M., Dewar, W.K., Berloff, P., Ward, M.L., 2011. Kelvin wave hydraulic control induced by interactions between vortices and topography. *J. Fluid Mech.* 687, 194–208. <http://dx.doi.org/10.1017/jfm.2011.344>.
- Ioannou, A., Stegner, A., Le Vu, B., Taupier-Letage, I., Speich, S., 2017. Dynamical evolution of intense ierapetra Eddies on a 22 year long period. *J. Geophys. Res. Oceans* 122, 9276–9298. <http://dx.doi.org/10.1002/2017JC013158>, <http://doi.wiley.com/10.1002/2017JC013158>.
- Ivanov, Y., Koroblev, A., 1995. Formation and regeneration of the pycnocline lens in the Norwegian Sea. *Russ. Meteorol. Hydrol.* 62–69.
- Klein, P., Hua, B.L., Lapeyre, G., Capet, X., Le Gentil, S., Sasaki, H., 2008. Upper ocean turbulence from high-resolution 3D simulations. *J. Phys. Oceanogr.* 38, 1748–1763.
- Köhl, A., 2007. Generation and stability of a Quasi-permanent vortex in the Lofoten basin. *J. Phys. Oceanogr.* 37, 2637–2651. <http://dx.doi.org/10.1175/2007JPO3694.1>.
- LaCasce, J.H., 1998. A geostrophic vortex over a slope. *J. Phys. Oceanogr.* 28, 2362–2381.
- Lam, J., Dritschel, D.G., 2001. On the beta-drift of an initially circular vortex patch. *J. Fluid Mech.* 436, 107–129. <http://dx.doi.org/10.1017/S0022112001003974>.

- Large, W., McWilliams, J., Doney, S., 1994. Oceanic vertical mixing: A review and a model with a nonlocal boundary layer parameterization. *Rev. Geophys.* 32, 363–403. <http://dx.doi.org/10.1029/94RG01872>.
- Le Corre, M., Gula, J., Smilena, A., Houpert, L., 2019. On the dynamics of a deep quasi-permanent anticyclonic eddy in the rockall trough. *Association FranÇAis de MÉCanique, Brest, France 12*.
- Le Corre, M., Gula, J., Tréguier, A.-M., 2020. Barotropic vorticity balance of the North Atlantic subpolar gyre in an eddy-resolving model. *Ocean Sci.* 16, 451–468. <http://dx.doi.org/10.5194/os-16-451-2020>.
- Le Vu, B., Stegner, A., Arsouze, T., 2018. Angular momentum Eddy detection and tracking algorithm (AMEDA) and its application to coastal Eddy formation. *J. Atmos. Ocean. Technol.* 35, 739–762. <http://dx.doi.org/10.1175/JTECH-D-17-0010.1>.
- Legg, S., McWilliams, J.C., 2001. Convective modifications of a geostrophic eddy field. *J. Phys. Oceanogr.* 31, 874–891.
- Legg, S., McWilliams, J., Gao, J., 1998. Localization of deep ocean convection by a mesoscale eddy. *J. Phys. Oceanogr.* 28, 944–970.
- Lilly, J.M., Rhines, P.B., Schott, F., Lavender, K., Lazier, J., Send, U., D'Asaro, E., 2003. Observations of the Labrador Sea eddy field. *Prog. Oceanogr.* 59, 75–176. <http://dx.doi.org/10.1016/j.pocean.2003.08.013>.
- de Marez, C., L'Hégaret, P., Morvan, M., Carton, X., 2019. On the 3D structure of eddies in the Arabian Sea. *Deep-Sea Res. I* <http://dx.doi.org/10.1016/j.dsri.2019.06.003>, <https://linkinghub.elsevier.com/retrieve/pii/S0967063718303650>.
- de Marez, C., Meunier, T., Morvan, M., L'Hégaret, P., Carton, X., 2020a. Study of the stability of a large realistic cyclonic eddy. *Ocean Model.* 146, 101540. <http://dx.doi.org/10.1016/j.ocemod.2019.101540>.
- de Marez, C., Meunier, T., Tedesco, P., L'Hégaret, P., Carton, X., 2020b. Vortex-wall interaction on the  $\beta$ -plane and the generation of deep submesoscale cyclones by internal Kelvin Waves-current interactions. *Geophys. Astrophys. Fluid Dyn.* 114, 588–606. <http://dx.doi.org/10.1080/03091929.2020.1772779>.
- McWilliams, J.C., 1985. Submesoscale, coherent vortices in the ocean. *Rev. Geophys.* 23, 165. <http://dx.doi.org/10.1029/RG023i002p00165>.
- Méneguen, C., Le Gentil, S., Marchesiello, P., Ducoffre, N., 2018. Destabilization of an oceanic meddy-like vortex: energy transfers and significance of numerical settings. *J. Phys. Oceanogr.* 48, 1151–1168. <http://dx.doi.org/10.1175/jpo-d-17-01261>.
- Mkhinini, N., Coimbra, A.L.S., Stegner, A., Arsouze, T., Taupier-Letage, I., Béranger, K., 2014. Long-lived mesoscale eddies in the eastern mediterranean sea: Analysis of 20 years of AVISO geostrophic velocities. *J. Geophys. Res. Oceans* 119, 8603–8626. <http://dx.doi.org/10.1002/2014JC010176>, <http://doi.wiley.com/10.1002/2014JC010176>.
- Nof, D., Dewar, W., 1994. Alignment of lenses: laboratory and numerical experiments. *Deep-Sea Res. I* 41, 1207–1229. [http://dx.doi.org/10.1016/0967-0637\(94\)90041-8](http://dx.doi.org/10.1016/0967-0637(94)90041-8).
- Perrot, X., Carton, X., 2010. 2D vortex interaction in a non-uniform flow. *Theor. Comput. Fluid Dyn.* 24, 95–100. <http://dx.doi.org/10.1007/s00162-009-0127-4>.
- Rodríguez-Marroyo, R., Viúdez, A., Ruiz, S., 2011. Vortex merger in oceanic tripole. *J. Phys. Oceanogr.* 41, 1239–1251. <http://dx.doi.org/10.1175/2011JPO4582.1>.
- Roulet, G., Capet, X., Maze, G., 2014. Global interior eddy available potential energy diagnosed from Argo floats. *Geophys. Res. Lett.* 41, 1651–1656. <http://dx.doi.org/10.1002/2013GL059004>.
- Schubert, R., Gula, J., Greatbatch, R.J., Baschek, B., Biastoch, A., 2020. The submesoscale kinetic energy cascade: Mesoscale absorption of submesoscale mixed layer eddies and frontal downscale fluxes. *J. Phys. Oceanogr.* 50, 2573–2589. <http://dx.doi.org/10.1175/JPO-D-19-0311.1>, arXiv:<https://journals.ametsoc.org/jpo/article-pdf/50/9/2573/4992078/jpod190311.pdf>.
- Shchepetkin, A.F., McWilliams, J.C., 2005. The regional oceanic modeling system (ROMS): a split-explicit, free-surface, topography-following-coordinate oceanic model. *Ocean Modell.* 9, 347–404.
- Shchepetkin, A.F., McWilliams, J.C., 2011. Accurate Boussinesq oceanic modeling with a practical, “stiffened” equation of state. *Ocean Modell.* 38, 41–70. <http://dx.doi.org/10.1016/j.ocemod.2011.01.010>.
- Smilena, A., Gula, J., Le Corre, M., Houpert, L.c., Reecht, Y., 2020. A persistent deep anticyclonic vortex in the rockall trough sustained by anticyclonic vortices shed from the slope current and wintertime convection. *J. Geophys. Res. Oceans* 125, <http://dx.doi.org/10.1029/2019JC015905>.
- Solodoch, A., Stewart, A.L., McWilliams, J.C., 2021. Formation of anticyclones above topographic depressions. *J. Phys. Oceanogr.* 51, 207–228. <http://dx.doi.org/10.1175/JPO-D-20-0150.1>.
- Sutyrin, G., 2019. On vortex intensification due to stretching out of weak satellites. *Phys. Fluids* 31, 075103. <http://dx.doi.org/10.1063/1.5098068>.
- Sutyrin, G., Radko, T., 2019. On the peripheral intensification of two-dimensional vortices in smaller-scale randomly forcing flow. *Phys. Fluids* 31, 101701. <http://dx.doi.org/10.1063/1.5118752>.
- Trodahl, M., Isachsen, P.E., Lilly, J.M., Nilsson, J., Kristensen, N.M., 2020. The regeneration of the lofoten vortex through vertical alignment. *J. Phys. Oceanogr.* 50, 2689–2711. <http://dx.doi.org/10.1175/JPO-D-20-0029.1>, URL: <https://journals.ametsoc.org/view/journals/phoc/50/9/jpoD200029.xml>.
- Verron, J., Hopfinger, E., McWilliams, J., 1990. Sensitivity to initial conditions in the merging of two-layer baroclinic vortices. *Phys. Fluids A* 2, 886–889. <http://dx.doi.org/10.1063/1.857647>.
- Verron, J., Valcke, S., 1994. Scale-dependent merging of baroclinic vortices. *J. Fluid Mech.* 264, 81–106. <http://dx.doi.org/10.1017/S0022112094000595>.
- Volkov, D.L., 2005. Interannual variability of the altimetry-derived eddy field and surface circulation in the extratropical north atlantic ocean in 1993–2001. *J. Phys. Oceanogr.* 35, 405–426. <http://dx.doi.org/10.1175/JPO2683.1>.
- White, M.A., Heywood, K.J., 1995. Seasonal and interannual changes in the north atlantic subpolar gyre from Geosat and TOPEX/POSEIDON altimetry. *J. Geophys. Res.* 100, 24931. <http://dx.doi.org/10.1029/95JC02123>.
- Xu, W., Miller, P.I., Quartly, G.D., Pingree, R.D., 2015. Seasonality and interannual variability of the European slope current from 20years of altimeter data compared with in situ measurements. *Remote Sens. Environ.* 162, 196–207. <http://dx.doi.org/10.1016/j.rse.2015.02.008>.
- Yu, L., Bosse, A., Fer, I., Orvik, K.A., Bruvik, E.M., Hessevik, I., Kvallsund, K., 2017. The lofoten basin eddy: Three years of evolution as observed by seagliders: THE LOFOTEN BASIN EDDY. *J. Geophys. Res. Oceans* 122, 6814–6834. <http://dx.doi.org/10.1002/2017JC012982>.
- Zhang, Z., Wang, W., Qiu, B., 2014. Oceanic mass transport by mesoscale eddies. *Science* 345, 322–324. <http://dx.doi.org/10.1126/science.1252418>.